Available online at www.sciencedirect.com

ScienceDirect

Physics Procedia 83 (2016) 26 – 35

Physics Procedia

9th International Conference on Photonic Technologies - LANE 2016

Optimization and simulation of SLM process for high density H13 tool steel parts

Petri Laakso[a,*], Tuomas Riipinen[a], Anssi Laukkanen[b], Tom Andersson[b], Antero Jokinen[a], Alejandro Revuelta[a], Kimmo Ruusuvuori[a]

[a]*VTT Technical Research Centre of Finland Ltd, Kemistintie 3, Espoo 02044, Finland*
[b]*VTT Technical Research Centre of Finland Ltd, Kivimiehentie 3, Espoo 02044, Finland*

Abstract

This paper demonstrates the successful printing and optimization of processing parameters of high-strength H13 tool steel by Selective Laser Melting (SLM). D-Optimal Design of Experiments (DOE) approach is used for parameter optimization of laser power, scanning speed and hatch width. With 50 test samples (1×1×1cm) we establish parameter windows for these three parameters in relation to part density. The calculated numerical model is found to be in good agreement with the density data obtained from the samples using image analysis. A thermomechanical finite element simulation model is constructed of the SLM process and validated by comparing the calculated densities retrieved from the model with the experimentally determined densities. With the simulation tool one can explore the effect of different parameters on density before making any printed samples. Establishing a parameter window provides the user with freedom for parameter selection such as choosing parameters that result in fastest print speed.

Peer-review under responsibility of the Bayerisches Laserzentrum GmbH

Keywords: Selective Laser Melting; optimization; density; design of experiments; finite element; simulation model; H13 tool steel

1. Introduction

Selective Laser Melting (SLM) is an Additive Manufacturing (AM) technology that is attracting the interest of the manufacturing industry with increasing pace. The most significant benefit of SLM compared to conventional

* Corresponding author. Tel.: +358-40-544-5646 ; fax: +358-20-722-7001 .
E-mail address: petri.laakso@vtt.fi

Peer-review under responsibility of the Bayerisches Laserzentrum GmbH
doi:10.1016/j.phpro.2016.08.004

manufacturing methods is the outstanding flexibility in part design that it offers. The growing demand for SLM in the manufacturing industry has increased the need for process development and parameter optimization for new powder materials in particular. In SLM a high power laser is used to melt a powder material layer by layer to create a solid part. The build process is controlled by changing the process parameters such as layer thickness, laser power, scanning speed and hatch width that all affect the build rate and properties of the finished part. For each SLM processed material a specific range of parameter combinations exist that result in sufficient quality, such as high density and desired surface roughness.

The optimal parameter window is practically always determined experimentally and there are different approaches for doing this. In the literature various approaches in process parameter optimization have been studied. Perhaps the most widely used approach is to conduct single track experiments followed by identification of the process parameters that result in suitable melt pool formation (Yadroitsev et al. (2010)). It is a common practice to limit the operational process parameter range by selecting upper and lower limits for a variable such as Volumetric Energy Density (VED) (Spierings et al. (2011)), which is based purely on theoretical predictions or observations from experimental tests such as single track experiments. The optimal parameters in terms of density can be determined experimentally by printing parts using different parameter combinations and determining the best parameters based on density measurements (Sander et al. (2016)). Also Design of Experiments (DOE) methods have been utilized for the optimization (Averyanova et al. (2011)). However, typically two or more of these approaches are combined to increase the effectiveness of the optimization process. (Gong et al. (2014)).

Ideally the optimization should be done with as little experimental work as possible or even entirely without experimental work to increase cost efficiency and speed of the process. This is where simulation models of the SLM process could play a major role. Modeling the SLM process in part scale can be beneficial in predicting responses such as residual stresses, deformations, geometric tolerances and material properties, as presented in (Denlinger et al. (2014)). Defect types and their generation based on mesoscale mechanisms has been addressed by (Baureiss et al (2014)), where discrete analysis means were utilized to study the local melting process. For the modeling to be a viable solution for evaluation of part performance in real applications, the simulation results must be obtained quickly and with reasonable computational capabilities (King et al. (2015)). The present research is focused on optimization of SLM process parameters for H13 tool steel using DOE followed by formation and validation of FE simulation model, focusing especially on predicting defect structures based on thermomechanical modeling of SLM. The applicability of the model as a valid optimization tool is evaluated.

2. Experimental methods

2.1. Materials and equipment

Commercial gas atomized H13 powder supplied by SLM Solutions GmbH was used for the production of the samples for density optimization. The powder proved to be spherical in shape by examinations with SEM. The particle size distribution was determined using Malvern laser diffraction analysis equipment. The analysis revealed that the particle size of the gas atomized powder was normally distributed. The particle size distribution is presented using $D_{(x)}$ values that indicate the volume fraction percentage (x) below particle size D. The D_{10}, D_{50}, and D_{90} values were measured as 22 µm, 33 µm and 50µm. The spherical shape and the relatively narrow particle size distribution resulted in good flowability, which is essential for even powder distribution during the build process. The nominal chemical composition of the power is shown in Table 1. Before processing with SLM the powder was dried at 50°C for approximately 12h.

The samples were built using SLM solutions 125HL machine, which has a fiber laser with maximum power output of 400W. The build chamber was filled with argon gas (purity level 99,996 %) before operation and a constant gas flow of 1,5 l/min was used during the experiment. Oxygen content in the build chamber was maintained below 0,1 vol% during the process. The samples were built directly on a S235 structural steel substrate, which was heated and kept at 200°C during the process to reduce the thermal gradient and the resulting thermal stresses in the material.

Table 1. Nominal chemical composition of the gas atomized H13 powder (values in wt%).

Fe	C	Mn	Si	Cr	Ni	Mo	V	Cu	P	Si	Ni	O
Bal.	0,410	0,420	1,060	5,000	0,040	1,340	0,990	0,010	0,008	0,006	0,050	0,020

The substrate plate functioned as a heatsink to allow heat to conduct away from the samples. A powder layer thickness of 30 µm was used for the experiments. The process parameters were set different for the core and the edge of the part to improve the surface quality and increase build speed.

2.2. Design of Experiments

Two sets of samples were printed for which the parameters were selected based on D-optimal experimental design. Each sample set consisted of 25 (1×1×1cm) samples that were printed on the baseplate without support structures to rule out any effect they might have on the finished part. Only core parameters of the test samples were optimized and these parameters were scanning speed, laser power and hatch width. The hatching pattern was 7,5mm stripes with 67 degree turn between layers. The energy delivered to the material is one of the most significant process variables in SLM as it affects the characteristic of the forming melt pool and ultimately the properties of the finished part. This energy is referred to as Volumetric Energy Density (VED) and it is described with the following equation

$$VED = \frac{P}{v \cdot h \cdot t} \tag{1}$$

where P is laser power, v is scanning speed, h is hatch width and t is layer thickness. (Spierings et al. (2011)) The VED is affected by material properties such as reflectivity and therefore the optimal operation range must be evaluated for each material. (Sander et al. (2016)) Non-optimal VED values lead to unfavorable results such as partially melted particles, inhomogeneous melt track formation and vaporization of alloyed elements. Based on experimental research found in the literature (Spierings et al. (2011)), an operating range of 50 J/mm³ – 100 J/mm³ for volume energy densities was chosen for the DOE experiments. The minimum and maximum values defined the confined window of experimentation within the operability region.

The parameter combinations for the design of experiments were calculated for two sets of 25 samples as that was the maximum amount that could be fitted on the substrate plate. For the first set the hatch width and scanning speed were the variables for the response function and scan speed and laser power for the second. For the first set the power was kept constant at 175 W, and for the second set the hatch width was kept constant at 0,1mm. In the experimental designs the range for the hatch width, scanning speed and laser power values was 90 µm -150 µm, 400 mm/s – 1200 mm/s and 100 W – 300 W. The laser parameter values for the two sample sets are presented in Table 2. Based on these constraints, a D-optimal design was created using Gosset (Sloane and Hardin (2003)) with a full quadratic polynomial equation as the candidate fitting function. After printing, the samples were EDM wire cut from the baseplate, then ground from the top for approximately 1mm and polished for optical microscopy imaging and Fiji image analysis (Image J). The image analysis is based on thresholded black vs. white pixels where the ratio of dark and white areas of an image is calculated giving the porosity value. The image analysis was performed over a center area ranging from 73mm² to 90 mm² of the samples and one image of each sample was analyzed. Therefore the edges of the parts were left out of the porosity measurement.

2.3. Simulation model

The principal elements of the thermomechanical FE SLM model are presented schematically in Fig. 1. The model is a simple unsupported block lying on a baseplate and the layers are deposited sequentially on its top surface following given process settings, the block initially comprising solely the powder bed (20×20×20 cm) or a section of it. The SLM process is solved using an implicit coupled thermomechanical solution, introducing finite strain incremental plasticity and transient formulation of the problem. Finite element mesh utilized for individual test cube

geometries is presented in Fig. 1. Adaptive time incrementation scheme is utilized, the max possible increment size limited to approximately the time it takes for the beam to move half a layer thickness. Due to the small size of the test problem parallel solution using the implicit solver is feasible, although not particularly efficient. The numerical model is modified layer-by-layer during the numerical solution to introduce subsequent powder layers via addition of new finite elements to the solution. The boundary conditions and heat source are coupled and modified accordingly during solution. The powder-to-solid transformation is incorporated by utilizing user defined fields and internal material variables, essentially introducing a level set interpolating the phase distribution as a specific field from powder to liquid and again during solidification. These fields are used to track the assignment of material properties depending on its present state during the solution via material user subroutines. Effects like shrinkage are not account for explicitly, rather an effective approach is adopted where the final layer thickness is utilized in the solution of the heat transfer and mechanical problems.

Heat transfer is accounted for with respect to top surface convection and radiation to build chamber atmosphere, conduction between the sample to the adjacent powder bed (via a convection boundary condition mimicking convection to an uniform temperature sink of chamber temperature). Heat transfer via conduction to base plate is accounted for, the initial condition of the simulation is an approximation of a state where numerous layers have already been built on top of the base plate and the thermal conditions in that regard have stabilized. Mechanically the system is considered rigidly fixed to the base plate. The beam heat source is assumed to have a Gaussian intensity profile, and its traverse during the solution is accounted for using a specific subroutine which contains information for constructing the scan vectors. The beam surface heat flux is specified according to (Dai and Shaw (2005)) as:

$$q(r) = \propto \cdot \frac{2P}{\pi\, r_0^2} e^{-2r^2/r_0^2} \tag{2}$$

where $\propto$ is laser energy absorptance given a value of 0,35 following work and SLM thermal analysis reviews carried out in (Roberts et al. (2009); Zeng et al. (2012)) and (Tolochko et al. (2003)). The laser power P and spot size r_0 are given their actual process values, and the heat flux is input to the model as a function of radial distance r measured from location of current beam center.

Problem is nonlinear due to finite strains as well as nonlinear thermal and mechanical material properties. The powder bed and solid phase properties are related with respect to density and thermal conductivity simply as

$$\rho_{powder} = (1-\varphi)\,\rho_{bulk} \tag{3}$$

and

$$\lambda_{powder} = (1-\varphi)\,\lambda_{bulk} \tag{4}$$

for powder bed porosity ϕ. The powder bed relative density is given an experience motivated approximate value of 0,5. During phase changes (solid to liquid or in reverse) thermal conductivity and specific heat are computed according to

$$\lambda = \phi\lambda_1 + (1-\phi)\,\lambda_2 \tag{5}$$

for thermal conductivity in phase transition from “1” to “2”, ϕ being the phase fraction of the transition, and for specific heat

$$c_p = \phi c_p^1 + (1-\phi) c_p^2 + L_i \frac{\partial f(\phi)}{\partial T} \tag{6}$$

where L_i is the latent heat of phase change "i" and $f(\phi)$ is a smoothened unit step function between the phase transformation. Latent heat of fusion is treated by via the relationship between enthalpy of the phase transformation and specific heat, i.e. the relationship between enthalpy and specific heat is given by

$$H = \int_T \rho \cdot c_p \, dT \tag{7}$$

Beyond available data linear extrapolation is utilized.

The heat transfer film coefficient at the top surface is given a value of 10 W/mK, the convection taking place to a sink represented by the build chamber temperature assumed to be constant. Radiation heat transfer is specified according to Stefan-Boltzmann law, surface emissivity is set to 0,77 following a more detailed evaluation in (Tolochko et al. (2003)).

The SLM process model generation is implemented as a Python module to VTT in-house multiscale modeling toolset, VTT ProperTune™ (VTT Technical Research Centre of Finland). The SLM process model is generated using an object oriented library, and interfaced to a finite element solver utilizing a separate module, which in current case is the Abaqus 6.14-1. This enables the generation of the user subroutines and the model itself with respect to scan strategies etc. without the need for user to manually work on the finite element model and its lengthy definition, but rather exploiting information obtained from the AM system itself.

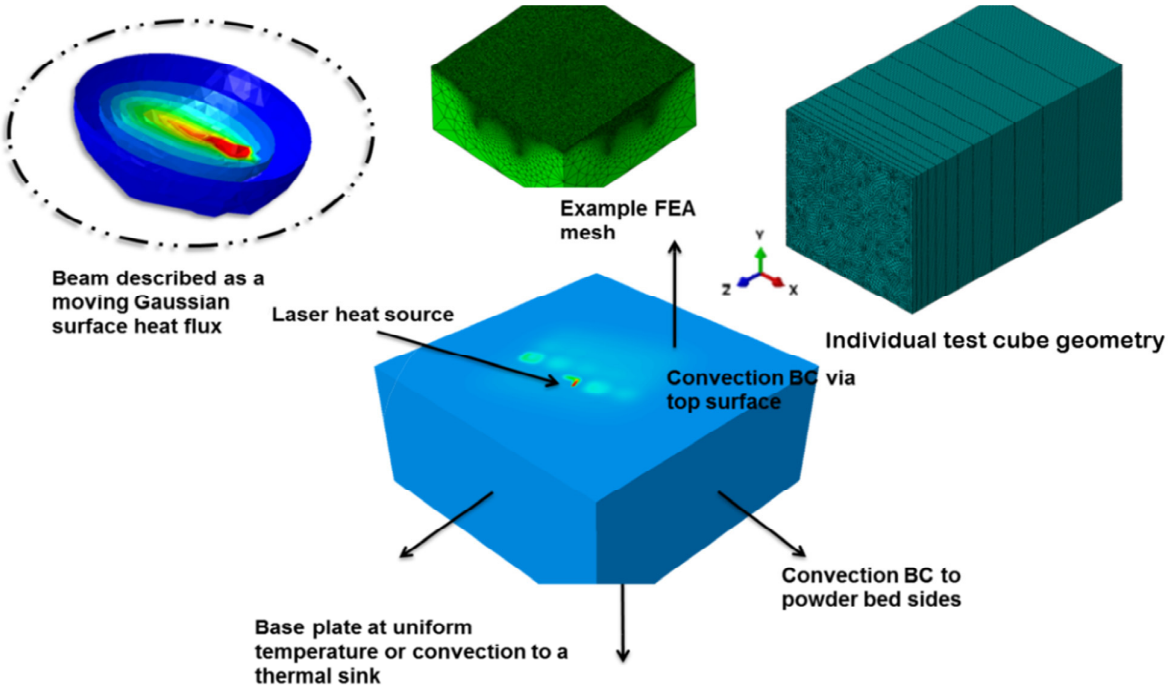

Fig. 1. The principal elements of the thermomechanical FE SLM model and Finite element mesh for individual test cube geometry.

3. Results

The process parameters and the porosity values of the printed test samples determined using image analysis are presented in Table 2. Micrographs were taken of the ground and polished samples using 1x and 5x magnifications for image analysis. There was a difference in the measured porosities between the images taken with 1x and 5x magnifications because the smallest pores were not detectable with lower magnification and the pores were not evenly distributed across the cross-section in all samples. The higher magnification provided a larger area for analysis and was therefore used in this paper. Since the combined area of the pores in the image analysis is based on threshold value, the appropriate threshold value had to be defined separately with each sample. Edge rounding of the pores was detectable after polishing, which acted as a source of error for the measurement.

Table 2. Process parameters and porosities of DOE samples.

Sample No. (DOE set 1.)	Speed (mm/s)	Hatch (µm)	VED (J/mm^3)	Porosity (%)	Sample No. (DOE set 2.)	Power (W)	Speed (mm/s)	VED (J/mm^3)	Porosity (%)
1	1050	108,91	51,01	6,38	1	144,1	960,7	50	5,55
2	450	126,01	102,87	0,8	2	100	666,7	50	12,74
3	899	107,02	60,63	0,5	3	180	1200	50	2,67
4	892,7	131,45	49,71	3,87	4	228,51	1200	63,48	0,23
5	618	150	62,93	0,63	5	100	400	83,33	1,87
6	1050	108,91	51,01	4,09	6	228,59	1200	63,5	0,24
7	640,1	109,28	83,39	0,11	7	139,85	636,9	73,19	0,25
8	828,2	90	78,26	0,17	8	160,4	534,7	99,99	0,06
9	899,1	107,38	60,42	0,49	9	300	1000	100	0,06
10	630,4	90	102,82	0,07	10	120	400	100	0,17
11	554,1	105,23	100,04	0,16	11	300	1200	83,33	0,15
12	739	132,62	59,52	0,79	12	234,05	936,1	83,34	0,14
13	609,3	135,19	70,82	0,18	13	241,53	805,1	100	0,13
14	450	150	86,42	0,82	14	300	1000	100	0,12
15	806,3	90	80,39	0,14	15	300	1200	83,33	0,14
16	583,5	133,38	74,95	0,22	16	205,89	686,3	100	0,24
17	656,4	107,42	82,73	0,11	17	180	1200	50	1,99
18	450	150	86,42	0,68	18	145,72	971,4	50	4,63
19	630,4	90	102,82	0,08	19	100	666,7	50	15,79
20	763,1	150	50,96	1,98	20	144,18	666,6	72,1	0,2
21	883,9	132,7	49,73	3,33	21	180	1200	50	3,48
22	763,1	150	50,96	1,93	22	100	400	83,33	6,09
23	1050	90	61,73	0,87	23	171,16	963,7	59,2	0,19
24	1050	90	61,73	0,69	24	250,51	993,7	84,03	0,09
25	450	126	102,88	0,56	25	135,83	623,6	72,61	0,17

A partial quadratic polynomial function was fitted to 80% of randomly selected data samples followed by validation of the result from the remaining 20%. For the first sample set the R^2 for the training samples was 0,907 and 0,901 for the validation ones. For the second sample set the R^2 was 0,968 and 0,951 respectively. Based on these results the calculated model can be effectively used to predict the density of printed H13 tool steel samples.

The fitted response surfaces (seen as contour plots in Fig.2) show the approximate response value (density) for the data points with different process variable combinations. The contour plots represent 2D planes in a 3D parameter space, where constraints related to process parameters were placed as explained in the previous chapter.

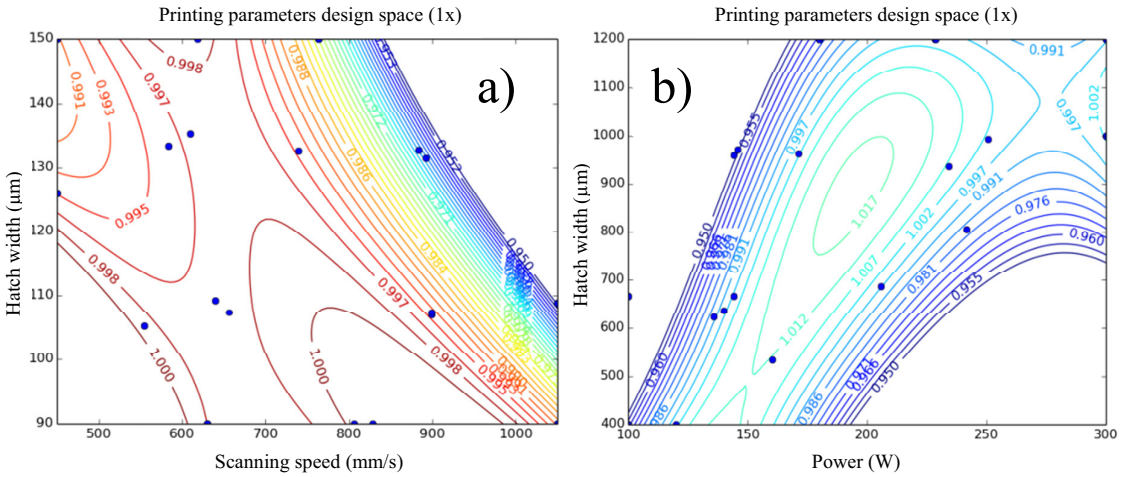

Fig. 2. (a) Density contour plot with hatch width and scanning speed as process variables (Power = 175W) and (b) Density contour plot with scan speed and power as process variables (Hatch width = 0,1 mm).

The effect of low and high VED values on the porosity of the samples is demonstrated by the micrographs taken from samples No.6 and No.11 from the first sample set (Fig 3. (a) –(b)). From the micrographs one can see that low energy density in the range of 50 J/mm^3 (Fig. 3 (a)) results in lack of fusion leading to high porosity (≥ 2%), whereas higher energy input of 100 J/mm^3 (Fig. 3 (b)) results in almost full density (99,84%). The micrographs in Fig.3 (c) – (d) show that high density parts can be printed using highly different process parameters. The power and scanning speeds of the samples in Fig.3 (c) and (d) are 160 W and 534,7 mm/s and 300 W and 1000 m/s. Both parameter combinations lead to 99,94% density and they both have a VED value approximately of 100 J/mm^3. The difference is the build speed which is almost doubled for the sample in Fig.3 (d).

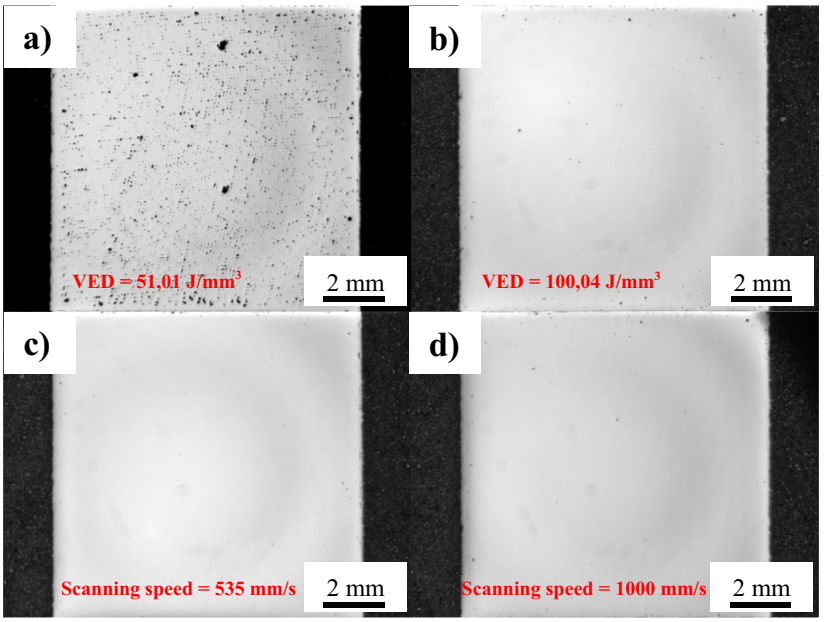

Fig. 3. Micrographs of samples No.6 (a) and No.11 (b) from the first DOE sample set and samples No.8 (c) and No.9 (d) from the second DOE sample set.

Samples No. 2, 3, 4, 11 and 24 from the second set were selected for closer simulation examinations. In Fig. 4 one can see the predicted porosity calculated from the simulation. The simulated parts are shown as white blocks next to the micrographs of actual printed parts built with same process parameters. The calculated porosities of the simulation models and the measured porosities are presented in Table 3.

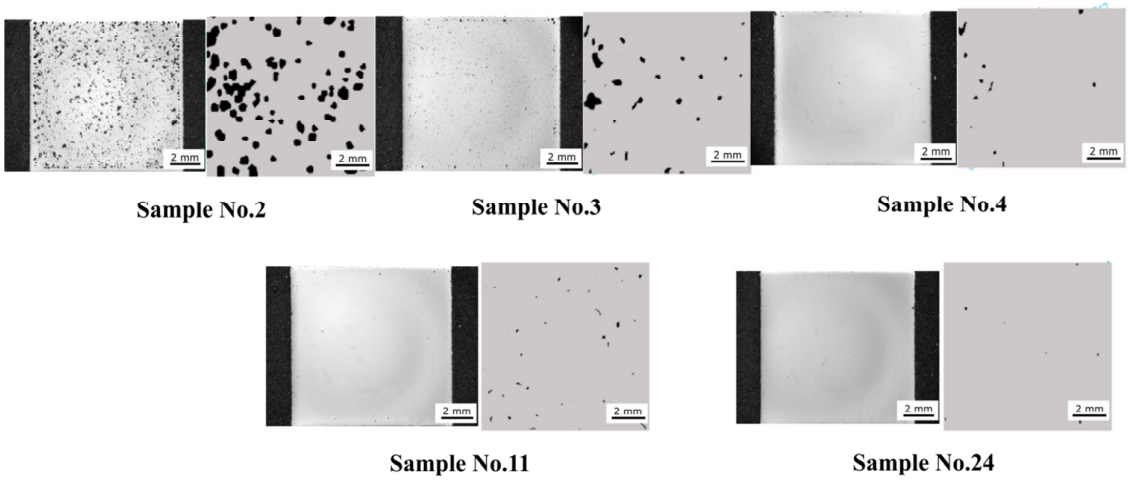

Fig. 4. Comparison of micrographs of DOE samples and simulated parts computed with same parameters (second sample set).

Table 3. Process parameters, measured porosities and calculated porosities of five DOE samples from second sample set.

Sample No.	Scanning speed mm/s	Power W	VED J/mm^3	Measured porosity (%)	Calculated porosity (%) (simulation model)
2	666,7	100	50	12,74	14,7
3	1200	180	50	2,67	2,7
4	1200	228,51	63,5	0,23	0,6
11	1200	200	83,3	0,15	0,4
24	993,7	250,51	84	0,09	0,08

4. Discussion

By comparing the measured porosities to the values obtained from the simulation, the similarity of the results is apparent. In fact the porosity decreases at the same rate for both the samples and the simulation model, when the VED increases. Despite the fact that the samples in our selected sample set (Table 3) show that density increases with larger VED values, the VED should not be used solely as a design parameter in process parameter optimization. The reason for this is that the optimal track geometry is achieved within certain range of scanning speed, power and hatch width and other process variables that are material dependent. The process parameters affect the melt pool characteristic and non-optimal process parameters can lead to lack of fusion and consequently lower density. Although a new layer partly melts the preceding layer, it is almost certain that points will still remain where the fusion of the consecutive layers is lacking (Yadroitsev et al. (2013)). The density of the printed parts is not influenced only by the chosen process parameters but also by the scanning strategy. There are many studies concerning the influence of different scanning strategies on the resulting quality of the finished parts (Su and Yang (2012); Thijs et al. (2013)). With decreasing hatch width the overlap between adjacent melt tracks is increased which reduces the likelihood of voids in the printed part.

On the basis of the data fitting presented in the Fig. 2 (b), it can be noted that high density parts can be produced even when the velocity of the laser beam is increased considerably, as long as the laser power is increased at the same time. This is because the melt pool geometry stays somewhat constant with higher scanning speed and power

values. At some point this analogy does not work anymore and the process becomes unstable. It is known that pores are commonly included inside melt pools which have keyhole geometry for high energy density input. This may be attributed to gas bubbles entrapped in the melt pool due to material(Pang et al. (2014)). Also very high velocities give rise to balling effects (Yadroitsev et al. (2010)). From Fig. 3 it can be seen that with hatch values higher than 100µm the region of high density becomes smaller meaning that there is less freedom with changing the velocity while still obtaining high density. Using a hatch width of 100µm allows one to have more freedom in selecting the scanning speed while maintaining almost full density. As the spot size, layer thickness and power are constant; choosing a scanning speed outside of the optimal region will affect the melt pool geometry leading to lower density. (Gong et al. (2014))

The utilized thermomechanical FE model was able to capture the porosity evolution during the investigated SLM parameter sets satisfactorily. The FE model yields mean-field like output since the defect generation mechanisms are not explicitly included, and as such the comparison and especially the trends which were obtained by tracking non-molten powder was adequate. Further explicit modeling of the powder bed at mesoscale is to be introduced to further tackle the mechanisms in a more physics-based manner. Obvious use for the SLM model is to carry out computational experiments in parallel with the experimental process development work to increase the rate of process development. In addition, due to the multitude of parameters the numerical models can be exploited to investigate complex parameter dependencies, and the outcomes can be evaluated using e.g. response surfaces. As such, the trends and interactions between process parameters become even easier to extract and visualize. Process and system design beyond current parameter spaces and transfer of system parameters between 3D printing machines are also possible means of exploitation. Also, it becomes possible to investigate and evaluate the significance of complex SLM process to material property causalities, by incorporating microstructural and mechanical modeling (Holmberg et al. (2014a); Holmberg et al. (2014b)), such as links between porosity, defect structures and resistance to fatigue crack initiation. Such exploitation of both modeling and experimental activities enables tighter integration of developments related to process, material and part design in pursuit of greater impact.

Regarding challenges to simulation of the SLM process the capability to retain high local resolution and to capture larger part scale material volumes remains an area were developments are direly needed. When utilizing current state-of-the-art solvers it would be beneficial to use a low resolution simulation model for the first round of parameter evaluation to save in computation pass-through time. The next round of simulation should have even higher resolution than what was tested to be able to predict porosity and related parameters of interest even better (residual stresses, phase maps etc.). Anyhow it seems that it is possible to make first tests only with simulation to shorten time needed to optimize the processing parameters. Still final testing needs to be done with actual printing trials to verify the optimal parameters. In addition, the treatment of powder bed physics and e.g. phase transformation kinetics is still quite simplified, particularly with respect to FE modeling a number of phenomena are treated in a mean-field and otherwise approximated manner.

5. Conclusions

SLM process parameters for H13 tool steel samples were optimized in relation to part density using D-optimal Design of Experiments approach. Analysis of the fitted functions showed that the predicted values fit the experimental data well as the obtained R^2 values indicate. This approach proved as a practical and reliable method for SLM parameter optimization. Within the studied parameter range one can easily examine the effect of different process parameters to the density. However evaluation of parameter combinations beyond the defined parameter planes requires more experimental work. According to the predicted response it is possible to select process parameters that increase the build rate significantly without compromising on the density. Based on the first sample set where the power was fixed at 175W it was found that with hatch width values below 120 µm the parameter window resulting in high density becomes wider. The probable reason behind this is the greater degree of overlap with the adjacent melt tracks, which decreases the occurrence of unmelted areas.

The developed finite element simulation model for the SLM process was verified by comparing the calculated densities to the experimentally obtained values. The model follows the same trend as the experimental results which demonstrate that the simulation could be used as a tool for parameter optimization. Future applications of the simulation model would be to use it for rough evaluation of optimal parameters for new powders in situations where

preliminary parameters are not available or for optimization between different SLM machines. However for more reliable results the model should be made more detailed. Next steps in the improvement of the parameter optimization would be to construct a parameter cloud, perform toughness tests and tensile test on samples built with optimal parameters to verify the validity of the results.

Acknowledgements

This study was carried out in the AM-teknologiasta uutta liiketoimintaa-project. The financial support of Tekes – the Finnish Funding Agency for Technology and Innovation and the participating industrial companies and the VTT Technical Research Centre of Finland is gratefully acknowledged.

References

Averyanova, M., Cicala, E., Bertrand, P., Grevey, D. 2011. Optimization of selective laser melting technology using design of experiments method. Innovative Developments in Virtual and Physical Prototyping: Proceedings of the 5th International Conference on Advanced Research in Virtual and Rapid Prototyping, Leiria, Portugal, 28 September-1 October, 2011, 459.

Baureiss, A., Scharowsky, T., Körner, C. 2014. Defect generation and propagation mechanisms during additive manufacturing by selective beam melting. Journal of Materials Processing Technology. 214, 2522-2528.

Dai, K., Shaw, L. 2005. Finite element analysis of the effect of volume shrinkage during laser densification. Acta Materialia. 53 18, 4743-4754.

Denlinger, E., Irwin, J., Michaleris, P. 2014. Thermomechanical modeling of additive manufacturing large parts. Journal of the Manufacturing Science and Engineering. 136, 1-8.

Gong, H., Gu, H., Zeng, K., Dilip, J., Pal, D., Stucker, B., Christiansen, D., Beuth, J., Lewandowski, J. J. 2014. Melt pool characterization for selective laser melting of ti-6Al-4V pre-alloyed powder. Solid Freeform Fabrication Symposium.

Holmberg, K., Laukkanen, A., Ghabchi, A., Rombouts, M., Turunen, E., Waudby, R., Suhonen, T., Valtonen, K., Sarlin, E. 2014a. Computational modelling based wear resistance analysis of thick composite coatings. Tribology International. 72 , 13-30.

Holmberg, K., Laukkanen, A., Turunen, E., Laitinen, T. 2014b. Wear resistance optimisation of composite coatings by computational microstructural modelling. Surface and Coatings Technology. 247 , 1-13.

King, W., Anderson, A., Ferencz, R., Hodge, N., Kamath, C., Khairallah, S., Rubenchik, A. 2015. Laser powder bed fusion additive manufacturing of metals; physics, computational, and materials challenges. Applied Physics Reviews. 2 4, 041304.

Pang, S., Chen, W., Wang, W. 2014. A quantitative model of keyhole instability induced porosity in laser welding of titanium alloy. Metallurgical and Materials Transactions A. 45 6, 2808-2818.

Roberts, I., Wang, C., Esterlein, R., Stanford, M., Mynors, D. 2009. A three-dimensional finite element analysis of the temperature field during laser melting of metal powders in additive layer manufacturing. International Journal of Machine Tools and Manufacture. 49 12, 916-923.

Sander, J., Hufenbach, J., Giebeler, L., Wendrock, H., Kühn, U., Eckert, J. 2016. Microstructure and properties of FeCrMoVC tool steel produced by selective laser melting. Materials & Design. 89 , 335-341.

Sloane, N., Hardin, R. 2003. Gosset: A General-Purpose Program for Designing Experiments.

Spierings, A., Herres, N., Levy, G. 2011. Influence of the particle size distribution on surface quality and mechanical properties in AM steel parts. Rapid Prototyping Journal. 17 3, 195-202.

Su, X., Yang, Y. 2012. Research on track overlapping during selective laser melting of powders. Journal of Materials Processing Technology. 212 10, 2074-2079.

Thijs, L., Kempen, K., Kruth, J., Van Humbeeck, J. 2013. Fine-structured aluminium products with controllable texture by selective laser melting of pre-alloyed AlSi10Mg powder. Acta Materialia. 61 5, 1809-1819.

Tolochko, N. K., Arshinov, M. K., Gusarov, A. V., Titov, V. I., Laoui, T., Froyen, L. 2003. Mechanisms of selective laser sintering and heat transfer in ti powder. Rapid Prototyping Journal. 9 5, 314-326.

VTT Technical Research Centre of Finland. ProperTune - Advanced computational modelling-based material design methodology. Retrieved from http://www.vttresearch.com/services/smart-industry/factory-of-the-future-%282%29/vtt-propertune%E2%84%A2-for-optimal-material-design.

Yadroitsev, I., Gusarov, A., Yadroitsava, I., Smurov, I. 2010. Single track formation in selective laser melting of metal powders. Journal of Materials Processing Technology. 210 12, 1624-1631.

Yadroitsev, I., Krakhmalev, P., Yadroitsava, I., Johansson, S., Smurov, I. 2013. Energy input effect on morphology and microstructure of selective laser melting single track from metallic powder. Journal of Materials Processing Technology. 213 4, 606-613.

Zeng, K., Pal, D., Stucker, B. 2012. A review of thermal analysis methods in laser sintering and selective laser melting. Proceedings of Solid Freeform Fabrication Symposium Austin, TX.